



Dependence of mid-ocean ridge morphology on spreading rate in numerical 3-D models

C. Püthe*, T. Gerya

ETH Zürich, Institute of Geophysics, Sonneggstrasse 5, 8092 Zürich, Switzerland

ARTICLE INFO

Article history:

Received 17 December 2012
 Received in revised form 2 April 2013
 Accepted 4 April 2013
 Available online 1 May 2013

Handling Editor: ARA Aitken

Keywords:

Mid-ocean ridge
 Spreading rate
 3-D thermomechanical modeling
 Oceanic core complexes

ABSTRACT

The morphology of natural mid-ocean ridges changes significantly with the rate of extension. Full spreading rate on Earth varies over more than one order of magnitude, ranging from less than 10 mm/yr at the Gakkel Ridge in the Arctic Ocean to 170 mm/yr at the East Pacific Rise. The goal of this study is to reproduce and investigate the spreading patterns as they vary with extension rate using 3-D thermomechanical numerical models. The applied finite difference marker-in-cell code incorporates visco-plastic rheology of the lithosphere and a crustal growth algorithm. The evolution of mid-ocean ridges from nucleation to a steady-state is modelled for a wide range of spreading rates. With increasing spreading rate, four different regimes are obtained: (a) stable alternating magmatic and amagmatic sections (≈ 10 mm/yr), (b) transient features in asymmetrically spreading systems (≈ 20 mm/yr), (c) stable orthogonal ridge-transform fault patterns (≈ 40 mm/yr) and (d) stable curved ridges (≥ 60 mm/yr). Modelled ultraslow and slow mid-ocean ridges share key features with natural systems. Abyssal hills and oceanic core complexes are the dominant features on the flanks of natural slow-spreading ridges. Numerically, very similar features are produced, both generated by localised asymmetric plate growth controlled by a spontaneous development of large-offset normal faults (detachment faults). Asymmetric accretion in our models implies a lateral migration of the ridge segment, which might help explaining the very large offsets observed at certain transform faults in nature.

© 2013 International Association for Gondwana Research. Published by Elsevier B.V. All rights reserved.

1. Introduction

The mid-ocean ridge is the longest mountain chain on Earth and one of the most prominent surface expressions of plate tectonics. The mostly perpendicular alignment of magmatic segments and transform faults is its most prominent feature. But the morphology of the ridge has a large variability around the globe and changes significantly with the rate of extension. Spreading rate on Earth varies between less than 10 mm/yr at the Gakkel Ridge in the Arctic Ocean (Dick et al., 2003) and 170 mm/yr at the East Pacific Rise (Macdonald, 2001).

The literature distinguishes between slow-spreading ridges (full spreading rates < 55 mm/yr), intermediate-spreading ridges (55–80 mm/yr) and fast-spreading ridges (> 80 mm/yr; e.g. Dick et al., 2003; Buck et al., 2005). Slow-spreading ridges are typically characterized by axial rift valleys and a general rough topography, while fast-spreading ridges typically have axial highs and a much smoother topography. Intermediate-spreading ridges can have axial highs, axial valleys and transitional morphologies represented by a faulted topography with neither axial high nor valley (Phipps Morgan and Chen, 1993). As pointed out by Kappel and Ryan (1986), the morphology of ridges with intermediate spreading rates can also vary through time. In spite of their differences, slow-, intermediate- and fast-spreading

ridges all show the orthogonal spreading pattern involving active transform faults.

However, this traditional classification is not sufficient to describe the whole ridge system, as parts of the mid-ocean ridge lack transform faults. Dick et al. (2003) described a class of ultraslow-spreading ridges (at full spreading rates < 20 mm/yr) that are characterized by a very rough topography, alternating magmatic and amagmatic segments and a lack of transform faults. In the amagmatic zones, plate separation is accommodated tectonically. On the other end of the spectrum, Naar and Hey (1989) observed that for full spreading rates > 145 mm/yr, transform faults are replaced by rotating microplates, propagating rifts or overlapping spreading centres.

The morphological characteristics of ultraslow-, slow- and fast-spreading ridges are a topic of ongoing discussion in the scientific literature. As changes in mid-ocean ridge morphology occur on time scales that are too long for direct observations, analogue and numerical models have been developed in order to reproduce the structures observed in nature and to study the evolution of these systems (see review paper by Gerya (2012) and references therein). Analogue studies (e.g. Oldenburg and Brune, 1972; Dauteuil et al., 2002) so far mainly concentrated on reproducing the spreading patterns observed in nature, while reproducing the general ridge morphology proved to be more difficult. In contrast, several 2-D numerical studies focussed on modelling the morphology of ridge cross sections. Using simplified models with a central dike, Buck et al. (2005) reproduced the general morphology of both fast- and slow-spreading ridges as well as off-axis fault structures

* Corresponding author. Tel.: +41 446323088.
 E-mail address: christoph.pueithe@erdw.ethz.ch (C. Püthe).

and showed how axial highs and valleys can form. A similar model was used by Tucholke et al. (2008) and Olive et al. (2010), who investigated the conditions for long-living detachment faults. These faults in turn are the prerequisite for oceanic core complexes (OCCs), elevated and corrugated massifs first observed at inside corners of ridge-transform intersections at slow-spreading ridges (e.g. Cann et al., 1997). Both studies used spreading rates of 50 mm/yr. A central accretion zone was also prescribed in the study by Ito and Behn (2008), which addressed the transition between fast and slow spreading, represented by the range of morphologies at intermediate spreading rates. Being 2-D, the studies cited in this paragraph had obvious advantages in examining the cross-axis morphology, but they could not investigate along-axis variations and especially the behaviour at ridge offsets.

Most 3-D models of mid-ocean ridges so far either focussed on the distribution of stress and strain (e.g. Behn et al., 2002) or on the thermal structure and crustal growth mechanisms (e.g. Gregg et al., 2009). A few recent studies also investigated the effects on topography. Allken et al. (2011, 2012) presented models of upper crustal extensional systems. The studies however rather addressed the phase of rifting, since crustal accretion was not implemented, and spreading velocity was set to 5 mm/yr only. Choi et al. (2008) investigated spontaneous transform fault development for a large range of spreading rates from 10 mm/yr to 100 mm/yr, but crustal accretion was neglected, and little topographic effects were presented. Gerya (2010a) investigated the spontaneous nucleation of transform faults at a single straight ridge using a thermomechanical 3-D model. Although accretion of oceanic crust was neglected, the presented morphology shared several key features with natural systems. Using an updated model, the subsequent study (Gerya, 2013) investigated the full evolution of an accreting extensional system from the rifting phase to a steady-state, but numerical experiments were performed for a narrow range of spreading rates between 38 mm/yr and 57 mm/yr.

In this study, we use the numerical code and model setup by Gerya (2013). The sensitivity analysis is extended by considering a wider range of spreading rates from ultraslow to fast and investigating their effects on the resulting ridge morphology. With this approach, we want to reproduce and explain the variety of mid-ocean ridge morphologies on Earth.

After a brief summary of the methods and a description of the numerical setup (Section 2), we present results for reference models at different spreading rates (Sections 3.1–3.4). The sensitivity of the modelled mid-ocean ridges to parameters other than spreading rate is discussed in Section 3.5. Section 4 focusses on asymmetric accretion and discusses the involved mechanisms observed in the models of this study. A summary of our results including a comparison with natural data and previous models is provided in Section 5.

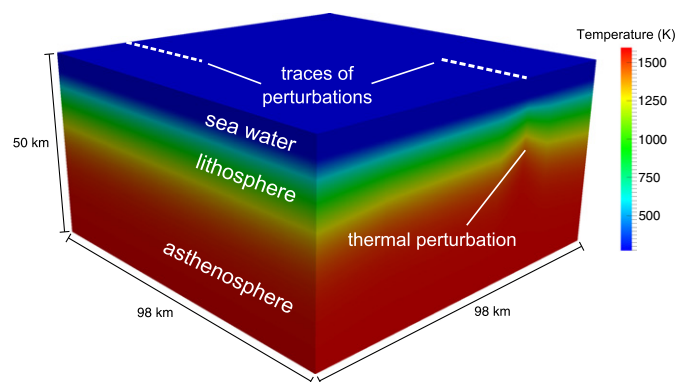


Fig. 1. Initial thermal structure of the model. The background profile is defined according to the cooling profile of a semi-infinite half-space (Turcotte and Schubert, 2002). The two thermal perturbations are arranged such that the model possesses a rotational symmetry about a vertical axis through its centre.

2. Numerical setup

The employed 3-D thermomechanical numerical code combines conservative finite differences on a fully staggered grid with the marker-in-cell technique. The Eulerian–Lagrangian model allows for large strains, strong localization of visco-plastic deformation and spontaneous growth of the oceanic crust by magma crystallization.

The rectangular Eulerian computational domain corresponds to a physical domain of $98 \times 98 \times 50$ km (Fig. 1, few models were run for a wider physical domain of $202 \times 98 \times 50$ km) and has a uniform nodal resolution of 0.5 km. 8 Lagrangian markers are inserted into each Eulerian cell and afterwards randomly distributed within the model domain. The conservation laws for momentum, mass and heat are solved with the thermomechanical code I3ELVIS (Gerya and Yuen, 2007) on the non-deforming Eulerian grid, whereas the advection of transport properties including viscosity, plastic strain, temperature etc. is performed by advecting the Lagrangian markers.

The initial model setup corresponds to the onset of oceanic spreading along an already thinned idealized rifted margin with 7–15 km thick crust. The initial thermal structure is defined according to the cooling profile of a semi-infinite half-space (Turcotte and Schubert, 2002). Similarly to previous numerical models of spontaneous plate fragmentation (e.g. Hieronymus, 2004; Choi et al., 2008; Allken et al., 2011, 2012), two thermal perturbations (hot seeds) with variable offset are imposed at the bottom of the lithospheric mantle (Fig. 1). Prescribing offset perturbations is consistent with observations on incipient oceanic spreading regions, where spreading segments nucleate en échelon in overlapping rift basins with non-transform spreading offsets (Taylor et al., 2009). A constant temperature boundary condition at the bottom of the model is used in most experiments.

Spreading is assumed to be caused by far-field tensional forces, implemented by prescribing constant normal velocities at the left and right lateral boundaries. Full spreading rates range between 10 mm/yr and 120 mm/yr. Lagrangian markers leave the Eulerian model domain through the left and right boundaries as they move with the flow. In order to ensure mass conservation, compensating influxes of sea water and mantle markers through the upper and lower boundaries of the domain, respectively, are prescribed. This Eulerian–Lagrangian numerical modelling scheme with open boundaries allows for an infinitely long plate separation with the use of a laterally limited Eulerian computational domain.

The model setup accounts for the following thermomechanical processes: thermal accretion of the mantle lithosphere, partial melting of the asthenospheric mantle, melt extraction and percolation towards the ridge, crystallization of the oceanic crust and hydrothermal circulation at the axis of the ridge. How these processes are implemented is described in Appendix A.

The model implies viscous rheology for the partially molten asthenosphere and visco-plastic rheology for the lithosphere. Viscosity of the asthenosphere is fixed to 10^{18} Pa s for the larger part of the models. In the other models, an experimentally determined dry olivine flow law (Ranalli, 1995) is applied for the viscosity of the asthenosphere. The dry olivine flow law is also used for the mantle lithosphere, whereas a plagioclase (An_{75}) flow law (Ranalli, 1995) is used for the viscous rheology of the crust. Details of the implementation of plastic yielding are described in Appendix B. Viscosity of the “sticky” ocean is set to 10^{18} Pa s. The large viscosity contrast to the underlying lithosphere generates an internal free surface. For numerical stability, the range of viscosity in the model is limited by upper and lower bounds (see Table 1).

3. Model results

A summary of the numerical experiments performed in this study and of the parameters that were varied is presented in Table 1. Detailed results for some representative experiments, differing in

Table 1
Summary of the models. The following parameters have been varied: Sp. rate—spreading rate, Nu —Nusselt number for hydrothermal circulation, η_{\min} and η_{\max} —minimum and maximum cutoff viscosities, η_{ast} —asthenospheric viscosity (with the arguments “fix” meaning constant low viscosity of 10^{18} Pa s and “var” meaning variable viscosity following the same flow law as the mantle lithosphere), Δx —offset between the initial thermal perturbations (the asterisk signifies that an additional oblique perturbation is prescribed), Width—model width, Crust—initial crustal thickness, BC_{th} —thermal boundary condition for the lower boundary of the model (with the arguments “flux” for a heat flux boundary condition or “XXXX K” for constant temperature), $\dot{\epsilon}_{\text{healing}}$ —fracture healing rate. Indices in the first column: ¹Fig. 6, ²Fig. 7, ³Fig. 5, ⁴Fig. 2. Abbreviations for the spreading patterns (last column): TF—transform fault, RMP—rotating microplate, ITSC—intra-transform spreading centre, AAZ—amagmatic accommodation zone.

Model	Sp. rate	Nu	η_{\min}	η_{\max}	η_{ast}	Δx	Width	Crust	BC_{th}	$\dot{\epsilon}_{\text{healing}}$	Spreading pattern
d1cm	10 mm/yr	2	10^{18} Pa s	10^{22} Pa s	fix	50 km	98 km	7 km	flux	10^{-13} s ⁻¹	AAZ btw. diverging magmatic segments
d2cm	19 mm/yr	2	10^{18} Pa s	10^{22} Pa s	fix	50 km	98 km	7 km	flux	10^{-13} s ⁻¹	Transient TF, straight ridge
d4cm ¹	38 mm/yr	2	10^{18} Pa s	10^{22} Pa s	fix	50 km	98 km	7 km	flux	10^{-13} s ⁻¹	Orthogonal ridge-TF pattern
d5cT	50 mm/yr	2	10^{18} Pa s	10^{22} Pa s	fix	50 km	98 km	7 km	1628 K	10^{-13} s ⁻¹	Ridge-TF pattern heading towards curved ridge
d5dT	50 mm/yr	2	10^{18} Pa s	10^{22} Pa s	fix	50 km	98 km	7 km	1598 K	10^{-13} s ⁻¹	Inclined ridge-TF pattern
d6cm	60 mm/yr	2	10^{18} Pa s	10^{22} Pa s	fix	50 km	98 km	7 km	flux	10^{-13} s ⁻¹	RMP, transient TF, curved ridge
d6dT	60 mm/yr	2	10^{18} Pa s	10^{22} Pa s	fix	50 km	98 km	7 km	1598 K	10^{-13} s ⁻¹	Transient TF, curved ridge
d8dT ²	80 mm/yr	2	10^{18} Pa s	10^{22} Pa s	fix	50 km	98 km	7 km	1598 K	10^{-13} s ⁻¹	Transient TF, curved ridge
d8fh	80 mm/yr	2	10^{18} Pa s	10^{22} Pa s	fix	50 km	98 km	7 km	1598 K	10^{-14} s ⁻¹	Transient TF, curved ridge
d8mT	80 mm/yr	2	10^{18} Pa s	10^{22} Pa s	fix	50 km	98 km	7 km	1610 K	10^{-13} s ⁻¹	Transient TF, curved ridge
d8uT	80 mm/yr	2	10^{18} Pa s	10^{22} Pa s	fix	50 km	98 km	7 km	1578 K	10^{-13} s ⁻¹	RMP, transient TF, curved ridge
d8ww	80 mm/yr	2	10^{18} Pa s	10^{22} Pa s	fix	80 km	202 km	7 km	1598 K	10^{-13} s ⁻¹	Two straight ridges
dXdT	100 mm/yr	2	10^{18} Pa s	10^{22} Pa s	fix	50 km	98 km	7 km	1598 K	10^{-13} s ⁻¹	Transient TF, curved ridge
dYcT	120 mm/yr	2	10^{18} Pa s	10^{22} Pa s	fix	50 km	98 km	7 km	1598 K	10^{-13} s ⁻¹	Transient TF, curved ridge
e4cm	38 mm/yr	2	10^{18} Pa s	10^{23} Pa s	var	40 km	98 km	7 km	1628 K	10^{-13} s ⁻¹	Transient TF, curved ridge
e4dT	38 mm/yr	2	10^{18} Pa s	10^{23} Pa s	var	40 km	98 km	7 km	1598 K	10^{-13} s ⁻¹	Inclined ridge-TF pattern
e8fh	80 mm/yr	2	10^{18} Pa s	10^{22} Pa s	fix	80 km*	202 km	7 km	1598 K	10^{-14} s ⁻¹	Transient ITSC and TFs, curved ridge
e8lv	80 mm/yr	2	10^{17} Pa s	10^{22} Pa s	fix	50 km	98 km	7 km	1598 K	10^{-13} s ⁻¹	Transient TF, curved ridge
e8mT	80 mm/yr	4	10^{18} Pa s	10^{22} Pa s	fix	50 km	98 km	7 km	1610 K	10^{-13} s ⁻¹	Orthogonal ridge-TF pattern
f1dT	10 mm/yr	4	10^{18} Pa s	10^{22} Pa s	fix	50 km	98 km	7 km	1598 K	10^{-13} s ⁻¹	AAZ btw. diverging magmatic segments
f2dT	19 mm/yr	4	10^{18} Pa s	10^{22} Pa s	fix	50 km	98 km	7 km	1598 K	10^{-13} s ⁻¹	Transient oblique TF and AAZ
f4dT	38 mm/yr	4	10^{18} Pa s	10^{22} Pa s	fix	50 km	98 km	7 km	1598 K	10^{-13} s ⁻¹	Transient TF, straight and curved ridge
f6dT	60 mm/yr	4	10^{18} Pa s	10^{22} Pa s	fix	50 km	98 km	7 km	1598 K	10^{-13} s ⁻¹	Orthogonal ridge-TF pattern
f8dT	80 mm/yr	4	10^{18} Pa s	10^{23} Pa s	var	40 km	98 km	7 km	1598 K	10^{-13} s ⁻¹	Growing RMP
f8wx	80 mm/yr	2	10^{18} Pa s	10^{22} Pa s	fix	80 km*	202 km	7 km	1598 K	10^{-13} s ⁻¹	Transient ITSC and TFs, curved ridge
h1vv	10 mm/yr	2	10^{18} Pa s	10^{23} Pa s	var	40 km	98 km	7 km	1598 K	10^{-13} s ⁻¹	Trough btw. stationary magmatic segments
h2lv ³	19 mm/yr	2	10^{18} Pa s	10^{22} Pa s	var	40 km	98 km	7 km	1598 K	10^{-13} s ⁻¹	Transient oblique TF and AAZ
h2sc	19 mm/yr	2	10^{18} Pa s	10^{23} Pa s	var	40 km	98 km	10 km	1598 K	10^{-13} s ⁻¹	Transient TF, oblique TF and AAZ
h2vv	19 mm/yr	2	10^{18} Pa s	10^{23} Pa s	var	40 km	98 km	7 km	1598 K	10^{-13} s ⁻¹	Transient TF, single ridge and AAZ
h6vv	60 mm/yr	2	10^{18} Pa s	10^{23} Pa s	var	40 km	98 km	7 km	1598 K	10^{-13} s ⁻¹	Transient TF, curved ridge
h8sc	80 mm/yr	2	10^{18} Pa s	10^{23} Pa s	var	40 km	98 km	10 km	1598 K	10^{-13} s ⁻¹	Transient TF, curved ridge
h8tc	80 mm/yr	2	10^{18} Pa s	10^{23} Pa s	var	40 km	98 km	15 km	1598 K	10^{-13} s ⁻¹	Growing RMP
k1ca	10 mm/yr	2	10^{18} Pa s	10^{22} Pa s	fix	30 km	98 km	7 km	flux	10^{-14} s ⁻¹	AAZ btw. diverging magmatic segments
k1cb	10 mm/yr	2	10^{18} Pa s	10^{22} Pa s	fix	30 km	98 km	7 km	flux	0 s ⁻¹	AAZ btw. diverging magmatic segments
k1cc	10 mm/yr	2	10^{18} Pa s	10^{23} Pa s	fix	30 km	98 km	7 km	flux	10^{-13} s ⁻¹	Transient AAZ and curved ridge
k1cd	10 mm/yr	8	10^{18} Pa s	10^{22} Pa s	fix	30 km	98 km	7 km	flux	10^{-13} s ⁻¹	AAZ btw. stationary magmatic segments
k1ce	10 mm/yr	2	10^{18} Pa s	10^{22} Pa s	fix	30 km	98 km	7 km	flux	10^{-12} s ⁻¹	AAZ btw. stationary magmatic segments
k1cm ⁴	10 mm/yr	2	10^{18} Pa s	10^{22} Pa s	fix	30 km	98 km	7 km	flux	10^{-13} s ⁻¹	AAZ btw. stationary magmatic segments
k1dT	10 mm/yr	2	10^{18} Pa s	10^{22} Pa s	fix	30 km	98 km	7 km	1598 K	10^{-13} s ⁻¹	AAZ btw. diverging magmatic segments
k1ncc	10 mm/yr	2	10^{18} Pa s	10^{23} Pa s	fix	50 km	98 km	7 km	1598 K	10^{-13} s ⁻¹	Trough btw. stationary magmatic segments
k1ncf	10 mm/yr	2	10^{18} Pa s	10^{24} Pa s	fix	50 km	98 km	7 km	1598 K	10^{-13} s ⁻¹	Trough btw. stationary magmatic segments
k1ncm	10 mm/yr	2	10^{18} Pa s	10^{22} Pa s	fix	50 km	98 km	7 km	1598 K	10^{-13} s ⁻¹	AAZ btw. diverging magmatic segments
k2ca	20 mm/yr	2	10^{18} Pa s	10^{22} Pa s	fix	30 km	98 km	7 km	flux	10^{-14} s ⁻¹	Transient TFs and single ridge
k2cb	20 mm/yr	2	10^{18} Pa s	10^{22} Pa s	fix	30 km	98 km	7 km	flux	0 s ⁻¹	Transient TFs and single ridge
k2cc	20 mm/yr	2	10^{18} Pa s	10^{23} Pa s	fix	30 km	98 km	7 km	flux	10^{-13} s ⁻¹	Transient TF, straight ridge
k2cd	20 mm/yr	8	10^{18} Pa s	10^{22} Pa s	fix	30 km	98 km	7 km	flux	10^{-13} s ⁻¹	Transient oblique TF and AAZ
k2ce	20 mm/yr	2	10^{18} Pa s	10^{22} Pa s	fix	30 km	98 km	7 km	flux	10^{-12} s ⁻¹	Single curved ridge
k2cm	20 mm/yr	2	10^{18} Pa s	10^{22} Pa s	fix	30 km	98 km	7 km	flux	10^{-13} s ⁻¹	Transient straight ridge, oblique TF
k2nca	20 mm/yr	2	10^{18} Pa s	10^{22} Pa s	fix	50 km	98 km	7 km	1598 K	10^{-14} s ⁻¹	Growing RMP
k2ncc	20 mm/yr	2	10^{18} Pa s	10^{23} Pa s	fix	50 km	98 km	7 km	1598 K	10^{-13} s ⁻¹	Unstable TF with variable offset
k2nce	20 mm/yr	2	10^{18} Pa s	10^{22} Pa s	fix	50 km	98 km	7 km	1598 K	10^{-12} s ⁻¹	Growing RMP
k2ncf	20 mm/yr	2	10^{18} Pa s	10^{24} Pa s	fix	50 km	98 km	7 km	1598 K	10^{-13} s ⁻¹	Unstable TF with variable offset
k2ncm	20 mm/yr	2	10^{18} Pa s	10^{22} Pa s	fix	50 km	98 km	7 km	1598 K	10^{-13} s ⁻¹	Unstable TF with variable offset
k2oce	20 mm/yr	2	10^{18} Pa s	10^{22} Pa s	fix	50 km*	98 km	7 km	1598 K	10^{-12} s ⁻¹	Orthogonal ridge-TF pattern with ITSC
k4ca	40 mm/yr	2	10^{18} Pa s	10^{22} Pa s	fix	30 km	98 km	7 km	flux	10^{-14} s ⁻¹	RMP
k4cb	40 mm/yr	2	10^{18} Pa s	10^{22} Pa s	fix	30 km	98 km	7 km	flux	0 s ⁻¹	RMP, curved ridge
k4cc	40 mm/yr	2	10^{18} Pa s	10^{23} Pa s	fix	30 km	98 km	7 km	flux	10^{-13} s ⁻¹	Transient TF, curved ridge
k4cd	40 mm/yr	8	10^{18} Pa s	10^{22} Pa s	fix	30 km	98 km	7 km	flux	10^{-13} s ⁻¹	TF with variable offset
k4ce	40 mm/yr	2	10^{18} Pa s	10^{22} Pa s	fix	30 km	98 km	7 km	flux	10^{-12} s ⁻¹	Single curved ridge
k4cm	40 mm/yr	2	10^{18} Pa s	10^{22} Pa s	fix	30 km	98 km	7 km	flux	10^{-13} s ⁻¹	Transient TF, curved ridge
k4nca	40 mm/yr	2	10^{18} Pa s	10^{22} Pa s	fix	50 km	98 km	7 km	1598 K	10^{-14} s ⁻¹	Orthogonal ridge-TF pattern
k4ncc	40 mm/yr	2	10^{18} Pa s	10^{23} Pa s	fix	50 km	98 km	7 km	1598 K	10^{-13} s ⁻¹	Orthogonal ridge-TF pattern
k4nce	40 mm/yr	2	10^{18} Pa s	10^{22} Pa s	fix	50 km	98 km	7 km	1598 K	10^{-12} s ⁻¹	Single curved ridge
k4ncf	40 mm/yr	2	10^{18} Pa s	10^{24} Pa s	fix	50 km	98 km	7 km	1598 K	10^{-13} s ⁻¹	Orthogonal ridge-TF pattern
k4ncm	40 mm/yr	2	10^{18} Pa s	10^{22} Pa s	fix	50 km	98 km	7 km	1598 K	10^{-13} s ⁻¹	Orthogonal ridge-TF pattern
k6dT	60 mm/yr	8	10^{18} Pa s	10^{22} Pa s	fix	50 km	98 km	7 km	1598 K	10^{-13} s ⁻¹	Unstable TF with variable offset
k6nca	60 mm/yr	2	10^{18} Pa s	10^{22} Pa s	fix	50 km	98 km	7 km	1598 K	10^{-14} s ⁻¹	Orthogonal ridge-TF pattern
k8cT	80 mm/yr	2	10^{18} Pa s	10^{22} Pa s	fix	50 km	98 km	7 km	1628 K	10^{-13} s ⁻¹	Transient TF, curved ridge
k8na	80 mm/yr	8	10^{18} Pa s	10^{22} Pa s	fix	40 km	98 km	7 km	1598 K	10^{-13} s ⁻¹	Unstable orthogonal ridge-TF pattern
k8nca	80 mm/yr	2	10^{18} Pa s	10^{22} Pa s	fix	50 km	98 km	7 km	1598 K	10^{-14} s ⁻¹	Transient TF, curved ridge

Table 1 (continued)

Model	Sp. rate	Nu	η_{\min}	η_{\max}	$\eta_{\text{ast.}}$	Δx	Width	Crust	BC_{th}	$\dot{\epsilon}_{\text{healing}}$	Spreading pattern
k8ncb	80 mm/yr	2	10^{18} Pa s	10^{22} Pa s	fix	50 km	98 km	7 km	1598 K	0 s^{-1}	Transient TF, curved ridge
k8ncc	80 mm/yr	2	10^{18} Pa s	10^{23} Pa s	fix	50 km	98 km	7 km	1598 K	10^{-13} s^{-1}	RMP
k8ncd	80 mm/yr	8	10^{18} Pa s	10^{22} Pa s	fix	50 km	98 km	7 km	1598 K	10^{-13} s^{-1}	RMP, transient irregular ridge, straight ridge
k8nce	80 mm/yr	2	10^{18} Pa s	10^{22} Pa s	fix	50 km	98 km	7 km	1598 K	10^{-12} s^{-1}	Transient TF, curved ridge
k8ncf	80 mm/yr	2	10^{18} Pa s	10^{24} Pa s	fix	50 km	98 km	7 km	1598 K	10^{-13} s^{-1}	RMP
k8ocd	80 mm/yr	8	10^{18} Pa s	10^{22} Pa s	fix	30 km	98 km	7 km	1598 K	10^{-13} s^{-1}	Orthogonal ridge-TF pattern
k8vfv	80 mm/yr	2	10^{18} Pa s	10^{22} Pa s	fix	50 km	98 km	7 km	flux	10^{-13} s^{-1}	Transient TF, curved ridge
kXvfv	100 mm/yr	2	10^{18} Pa s	10^{22} Pa s	fix	50 km	98 km	7 km	flux	10^{-13} s^{-1}	Transient TF, curved ridge
l1cm	10 mm/yr	2	10^{18} Pa s	10^{22} Pa s	fix	14 km	98 km	7 km	flux	10^{-13} s^{-1}	Curved ridge with narrow AAZ
m1cm	10 mm/yr	2	10^{18} Pa s	10^{22} Pa s	fix	0 km	98 km	7 km	flux	10^{-13} s^{-1}	Straight ridge with narrow AAZ
n1cT	10 mm/yr	2	10^{18} Pa s	10^{22} Pa s	fix	40 km	98 km	7 km	1628 K	10^{-13} s^{-1}	AAZ btw. diverging magmatic segments

the rate of extension, are presented in the following sections. These reference models have been computed with Nusselt number $Nu = 2$ (describing the extent of hydrothermal circulation, cf. Appendix A), viscosity limits of $\eta_{\min} = 10^{18}$ Pa s and $\eta_{\max} = 10^{22}$ Pa s, a fracture healing rate of $\dot{\epsilon}_{\text{healing}} = 10^{-13} \text{ s}^{-1}$ (cf. Appendix B) and an initial crustal thickness of 7 km. The identifiers of the models in Table 1 (first column) will be used as reference in the following sections.

3.1. Evolution of an ultraslow-spreading ridge model

Fig. 2 presents the evolution of the ultraslow-spreading reference model *k1cm*, which has a full spreading rate of 10 mm/yr. In the initial stage of spreading (Fig. 2a), extension generates numerous normal faults in the brittle lithosphere, which are especially concentrated above the magma chambers that formed due to partial melting in the thermally perturbed regions of the model. Two offset graben structures form atop the magma chambers. This stage is common for all models in this study.

The subsequent evolution is characterized by the development of two distinctly different zones. In the magmatic segments, new crust is generated due to symmetric accretion of melt at the walls of the magma chambers (Fig. 2b). As the magma chambers are situated several kilometres below sea floor, the newly generated crust is very thick. The addition of hot, low-density material causes a long-range uplift of the sea floor. The lithosphere breaks just above the axis of spreading, leading to the formation of a deep trench. The combination of both effects generates an approximately 40 km wide ridge with characteristic axial valley (Fig. 2c). In the zone between the magmatic segments, extension is fully compensated tectonically, i.e. by crustal thinning along numerous faults. The sea floor in this amagmatic zone is depressed, a trench connects the axial valleys of the magmatic segments (Fig. 2c).

Fig. 2e shows the steady state. Off-axis faulting causes a thinning of the initially very thick crust in the magmatic segments. The fault scarps are visible at the surface. They curve towards the amagmatic zone, thus slip on the faults is not purely extensional, but transtensional. Topography is generally rough and dominated by the elevated magmatic ridge segments with distinct axial valleys. In the amagmatic zone, in which the crust has completely disappeared and mantle is exposed to the sea floor, the plate boundary is defined by a depressed region, obliquely oriented to the direction of spreading.

3.2. Evolution of an asymmetrically accreting slow-spreading ridge model

At full spreading rates of about 20 mm/yr, ridge models exhibit an intermediate behaviour between slow and ultraslow spreading. The complex history of (mainly asymmetric) accretion can involve orthogonal and oblique transfer faults as well as straight ridges, zero-offset fracture zones and amagmatic accommodation zones.

The evolution of the reference model *h2lv*, which has a full spreading rate of 19 mm/yr, is depicted in Fig. 3.

In comparison to most ultraslow-spreading ridge models (cf. Section 3.1), the grabens developing above the imposed thermal perturbations are deeper and more pronounced. Extension is compensated tectonically by slip on one of the graben-bounding normal faults. This allows a rise of the magma chamber (schematically depicted in Fig. 4). A heavily faulted accommodation zone is established between the propagating spreading centres. The magmatic segments finally connect by a vertical proto-transform fault, which is slightly oblique to the direction of spreading (Fig. 3b). A deep, elongated depression marks this fault at the surface.

Extension is partially accommodated by crystallization (i.e. freezing of magma at the walls of the magma chamber) and partially by slip on major faults, which develop atop the magma chambers (cf. vertical cross section of the viscosity field in Fig. 3b). A close-up of the involved mechanisms is presented in Fig. 5a–b. The newly formed fault roots above the crest of the magma chamber. New crust is accreted in approximately equal proportions to footwall and hanging wall, and the magma chamber is stationary (Fig. 5a). In the further evolution, the fault moves to the right (i.e. with the hanging wall) due to the ongoing extension, until it roots close to the outer edge of the magma chamber. New crust is accreted to the footwall and experiences uplift at the fault. The magma chamber is in this process dragged towards the fault (Fig. 5b). The motion of the fault to the right represents a slow migration of the spreading centre. This causes asymmetric accretion with the left plate (footwall side) growing faster than the right plate (hanging wall side).

When conditions for further displacement on a fault become unfavourable, it is abandoned and a new fault forms within the newly accreted crust. The new fault can dip in the same direction as its predecessor, thus continuing the sense of asymmetric accretion (Figs. 3b and 5a–b), or in the opposite direction, thus changing its sense (Figs. 3e and 5a). This reorganisation of the spreading system, which implies a sudden lateral migration of the ridge segment, is the cause of the ridge-parallel hill structures visible in the bathymetry plots of Fig. 3b–e (first column). In particular, the densely spaced hills on the retreating plate (hanging wall side) are separated by abandoned faults.

At $t \approx 3.1$ Myr (in reference model *h2lv*, Fig. 3b), the two ridge segments begin to migrate inward toward each other due to the asymmetric accretion described above. The connecting proto-transform fault rotates, its sense of shearing thereby changes from transtensional to pure extension (Fig. 3c, viscosity plots). The former proto-transform fault, which can now be described as detachment fault, constitutes the plate boundary between the ridge segments. Massive displacement on the fault culminates in the exposure of mantle to the sea floor. Meanwhile, the fracture zone, which is a remnant of the phase of oblique spreading, is transported away from the ridge.

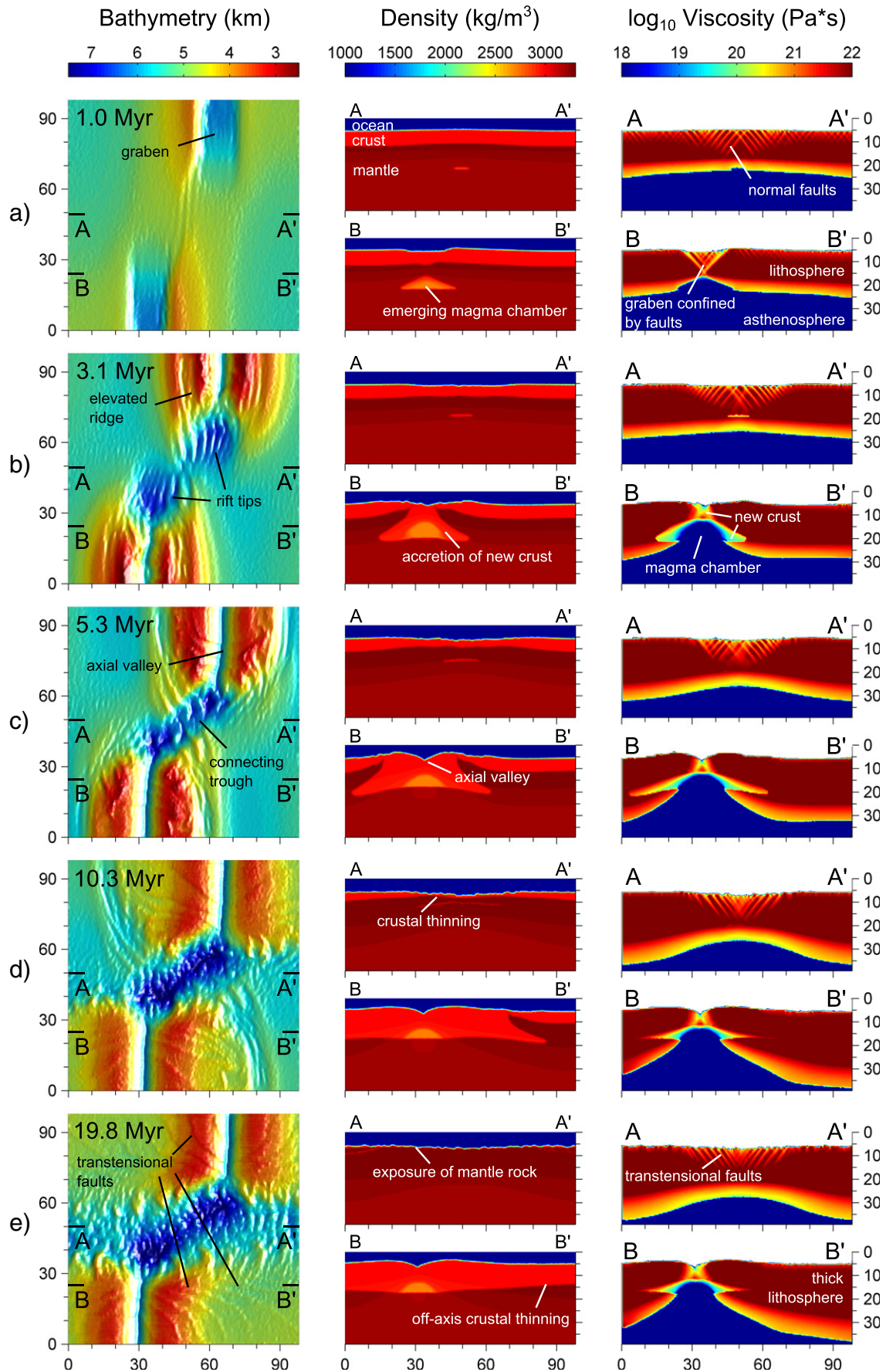


Fig. 2. Evolution of the ultraslow-spreading ridge model *k1cm*. Sea level for bathymetry maps (first column) corresponds to the top of the model. Note that a rheological model with constant viscosity in the asthenosphere is employed, cf. Appendix B.

The further evolution of the reference model *h2lv* shows that differential asymmetric accretion within a magmatic segment can lead to its bisection (almost happening at $t \approx 12.0$ Myr, cf. Fig. 3d). Note that this process has also been observed by Gerya (2010a) and in other models of this study, e.g. *h2vv*. Although ongoing asymmetric accretion reduces the offset between the ridge segments in model *h2lv*, the magma chambers do not connect. Instead, extension is accommodated tectonically in an amagmatic zone, and mantle is exposed to the sea floor over large regions (for a slightly different choice of

parameters, the magma chambers do connect and a single straight ridge is established, e.g. in model *d2cm*). Further asymmetric accretion eventually leads to the establishment of a new proto-transform fault, at which the sense of shearing is opposite to the original fault (Fig. 3e).

3.3. Evolution of a symmetrically accreting slow-spreading ridge model

Symmetrical spreading in an orthogonal ridge-transform fault system is the preferred mode of extension at slightly greater spreading rates of

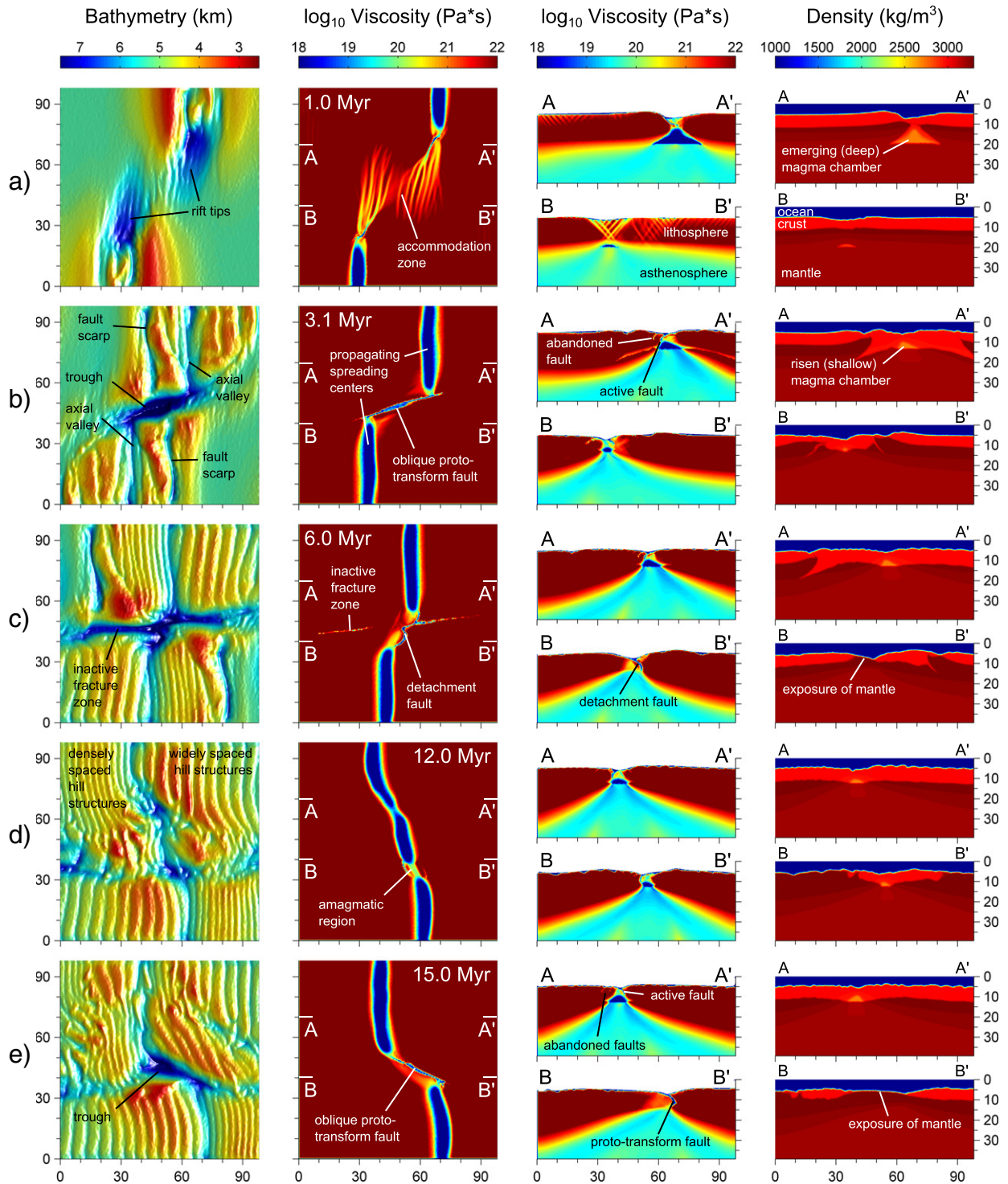


Fig. 3. Evolution of the asymmetrically accreting slow-spreading ridge model *h2lv*. Sea level for bathymetry maps (first column) corresponds to the top of the model. Horizontal cross sections for the viscosity field (second column) are taken at the level of 11 km from the top of the model. Note that the rheological model of the asthenosphere employs a dry olivine flow law (Ranalli, 1995), cf. Appendix B.

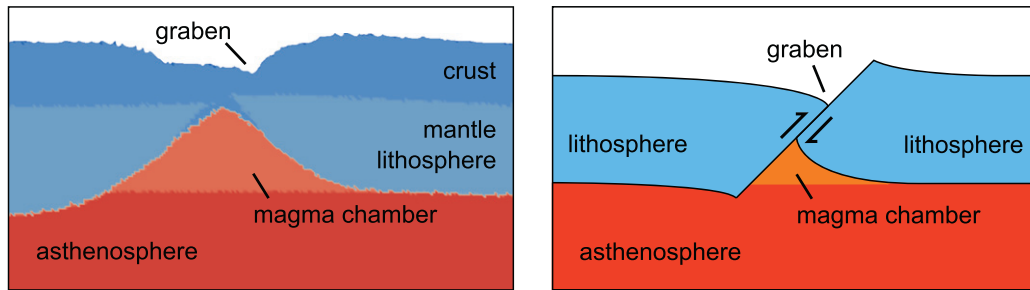


Fig. 4. Left panel: Composition, vertical slice of a ridge model around a magma chamber in the initial stage of spreading (model *d4cm*, $t = 0.3$ Myr). Right panel: Schematic representation of the processes in this stage of spreading. Extension is compensated by slip on a fault, a deep trench develops and the magma chamber rises.

about 40 mm/yr (for moderate fracture healing rates and initial offsets of 40–60 km). This has been shown by Gerya (2013) and is for completeness repeated in Fig. 6 for the reference model *d4cm*, which has a full spreading rate of 38 mm/yr.

In contrast to the previously shown model *h2lv*, the spreading centres in model *d4cm* continue to lengthen by ridge propagation after establishment of the proto-transform fault, but the ridge segments

do not migrate laterally (in the direction of spreading; Fig. 6b). The proto-transform fault rotates until it is parallel to the direction of spreading (Fig. 6c). Since the magmatic segments do not move, the established orthogonal pattern is stable. In steady-state, the orthogonal ridge-transform fault system is characterized by a gently depressed axial valley, bounded by flanks that are slightly elevated with respect to the distal sea floor, a depressed active transform fault that terminates in an inactive fracture zone, and numerous ridge-parallel hill structures of short wavelength (about 1 km).

A close-up of the viscosity field around the magma chamber (Fig. 5c) indicates a very similar structure as observed for asymmetrically accreting ridges (Fig. 5a–b). But the (comparably short) fault rooting close to the edge of the magma chamber is not active, and new crust is added in equal proportions to both plates. We conclude that axial faults in symmetrically accreting slow-spreading ridge models are short-lived structures that are frequently abandoned, therefore generating densely spaced hill structures. As the dip of the faults alternates through time and spreading is at most times accommodated without involvement of an axial fault, no net movement of the ridge is observed.

3.4. Evolution of a fast-spreading ridge model

Fig. 7 presents the evolution of the fast-spreading reference model *d8dT*, which has a full spreading rate of 80 mm/yr. Its initial development is very similar to that of the symmetrically accreting ridge model *d4cm* presented in the previous subsection. The evolution is however faster, the lithosphere is thinner and the cross section of the magma chambers is larger (compare with Fig. 6). A small rotating microplate develops in this particular model in the young spreading centres (Fig. 7a). It is however quickly attached to one of the plates and transported away from the ridge axis (Fig. 7c).

The orthogonal ridge-transform fault pattern observed in symmetrically accreting slow-spreading ridge models is only a transient feature in fast-spreading ridge models. The tips of the magmatic segments bend towards each other (Fig. 7c) until the magma chambers coalesce (Fig. 7d). A curved ridge, composed of orthogonally and obliquely spreading sections, is established (Fig. 7e). The topography of the system in steady-state is very smooth (or any faults that would form in this setting are too small to be resolved by the current model grid). The ridge flanks are slightly elevated with respect to the distal sea floor (max. 1 km). The ridge axis is marked by a gently depressed zone. As spreading is symmetric, no ridge-parallel hill structures develop (or their wavelength is below the model resolution).

3.5. Sensitivity to model parameters

As presented in the previous subsections, the morphology of mid-ocean ridge models in this study is mainly controlled by the imposed spreading rate. With increasing spreading rate, four regimes can be

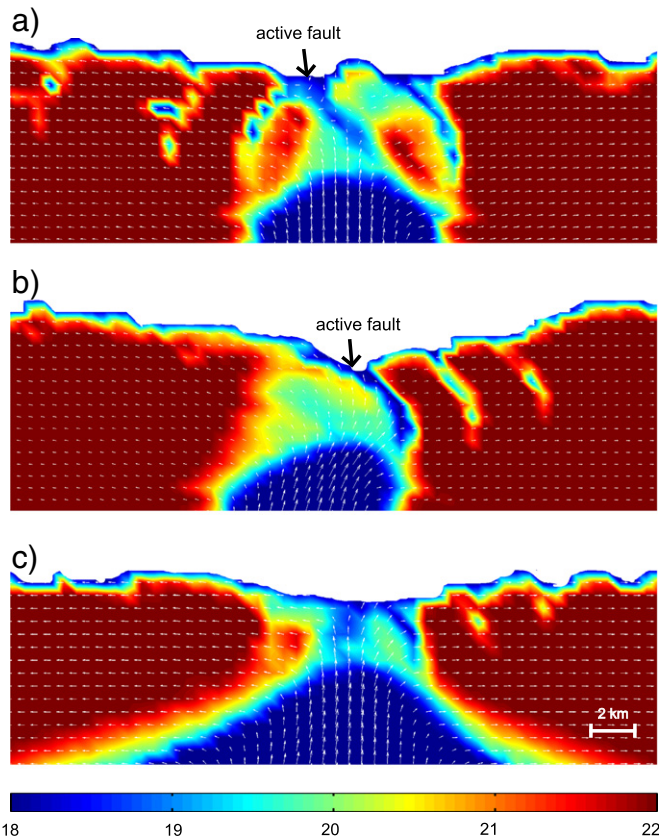


Fig. 5. a)–b) Close-ups of the $\log(\text{viscosity})$ field of an asymmetrically accreting ridge model around a magma chamber (model *f4dT*, $t = 5.3$ – 5.6 Myr). Arrows denote movement of the material. Newly created crust is uplifted at the fault, the magma chamber is dragged towards it. No movement occurs along the abandoned faults inside the plates. c) Close-up of the $\log(\text{viscosity})$ field of a symmetrically accreting ridge model around a magma chamber (model *d4cm*, $t = 3.3$ Myr). The fault atop the magma chamber is already abandoned, spreading is symmetric. Note that the blue (low-viscosity) zone in the bottom of each panel represents the magma chamber.

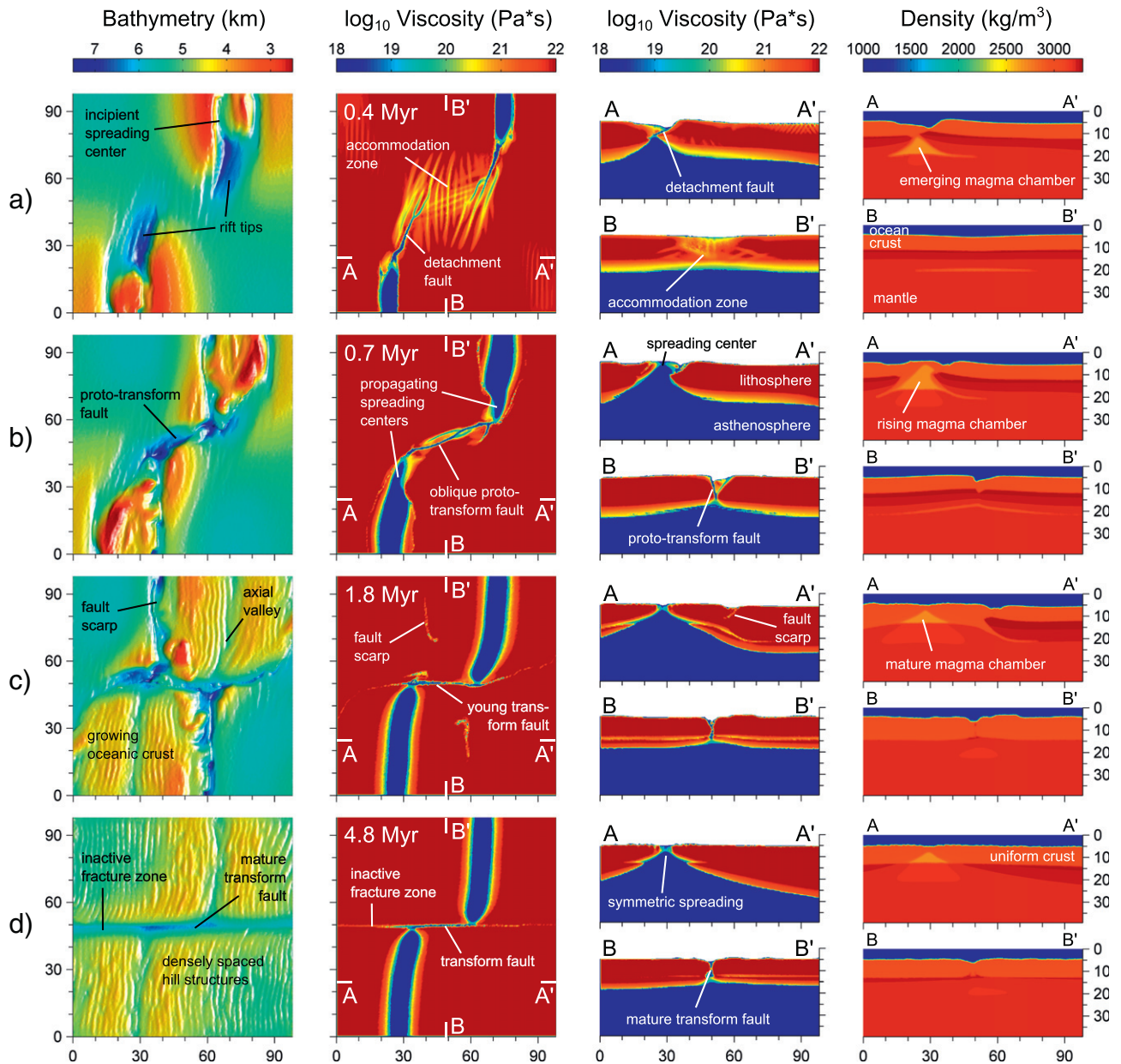


Fig. 6. Evolution of the symmetrically accreting slow-spreading ridge model *d4cm*. Sea level for bathymetry maps (first column) corresponds to the top of the model. Horizontal cross sections for the viscosity field (second column) are taken at the level of 10 km from the top of the model. Note that a rheological model with constant viscosity in the asthenosphere is employed, cf. Appendix B.

distinguished: (a) stable alternating magmatic and amagmatic sections, (b) transient features in asymmetrically spreading systems, (c) stable orthogonal ridge-transform fault patterns and (d) stable curved ridges. Gradual transitions between the different regimes, i.e. transient amagmatic segments as intermediate stage between regimes (a) and (b) or inclined ridge-transform patterns as intermediate stage between regimes (c) and (d), are also observed.

The extent of hydrothermal cooling in the crust is controlled by the Nusselt number Nu , cf. Appendix A. Increasing Nu has a similar effect as decreasing the spreading rate. This is easily understood from the impact of both parameters on the thermal structure of a (initially hot) lithospheric plate: At the same distance from the ridge axis, a fast-moving plate is hotter than a slow-moving plate, unless it is cooled down by increased hydrothermal activity. The diagram in Fig. 8 (left panel)

summarizes the interconnections between spreading rate, Nu and ridge morphology.

Gerya (2013) showed that the fracture healing rate $\dot{\epsilon}_{\text{healing}}$ has a significant influence on the modelling results. We performed a more systematic analysis of the interconnections between spreading rate, $\dot{\epsilon}_{\text{healing}}$ and the ridge morphology. Increasing $\dot{\epsilon}_{\text{healing}}$ decreases the average lifetime of faults and vice versa. This in particular has the effect that curved ridges (lacking transform faults) are favoured over stable orthogonal ridge-transform fault systems at high healing rates, cf. Fig. 8 (right panel). At high rates of spreading and healing, transform faults exist as transient features during initial to intermediate stages of spreading. In ultraslow-spreading ridge models, a reduced healing rate favours the formation of large-offset normal faults. Spreading is in the amagmatic zone thus accommodated by slip on one dominant

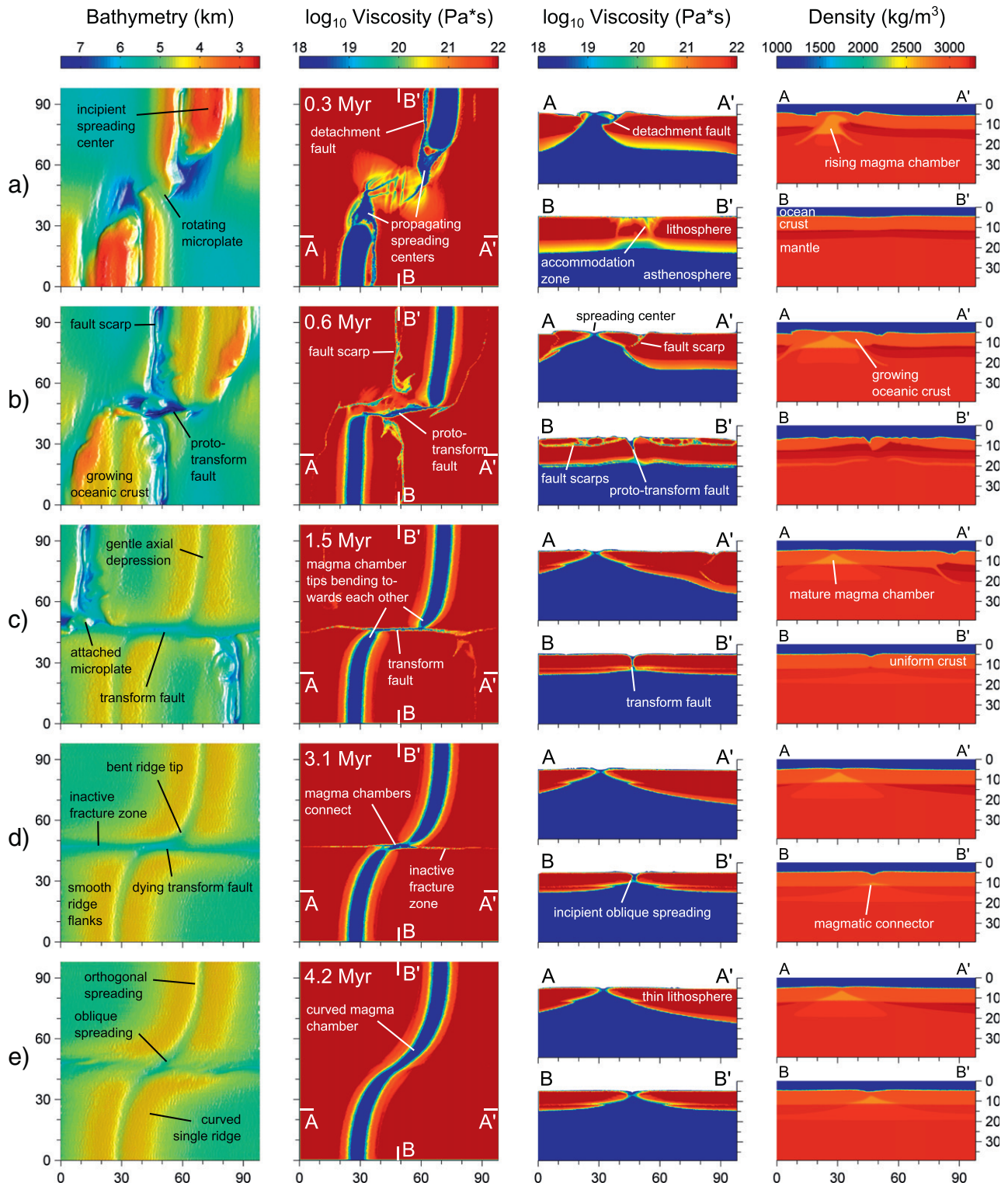


Fig. 7. Evolution of the fast-spreading ridge model *d8dT*. Sea level for bathymetry maps (first column) corresponds to the top of the model. Horizontal cross sections for the viscosity field (second column) are taken at the level of 8 km from the top of the model. Note that a rheological model with constant viscosity in the asthenosphere is employed, cf. Appendix B.

large-offset fault (and not by distributed faulting as in the model *k1cm* depicted in Fig. 2).

The influence of other parameters on the spreading mode is less significant, but they can have relevant influence on the ridge morphology:

- Small offsets between the thermal perturbations facilitate their connection and the formation of a single ridge, while large offsets

can impede a connection. This observation confirms the findings by Gerya (2013), who described the development of spreading centres with an intermediate growing (and sometimes rotating) plate in slow-spreading ridge models with large initial offset (≥ 60 km). In slow-spreading ridge models, the orthogonal ridge-transform fault system is only stable for initial offsets ≥ 40 km. In fast-spreading ridge models, the lifetime of transform faults has a positive correlation with the initial offset.

- The initial thickness of the crust has minor effects. A thicker crust mainly yields larger initial magma chambers, but does not affect the long-term evolution of the mid-ocean ridge system.
- A high maximum cut-off viscosity promotes massive displacement on a single fault, whereas a low maximum cut-off viscosity promotes a partitioning of the displacement on various faults in an accommodation zone. This mainly affects slow- and ultraslow-spreading ridges. A high maximum cut-off viscosity favours the formation of near-axis normal faults at ultraslow spreading rates (and thus has a similar effect as a reduced healing rate). The resulting models combine features of ultraslow-spreading ridges and asymmetrically accreting slow-spreading ridges, the amagmatic zone is dominated by a deep trough (e.g. model *k1ncc*). A high maximum cut-off viscosity also reduces the elevation of the ridge flanks with respect to the surrounding seafloor.
- The rheological model of the asthenosphere has minor impacts on the resulting morphology. If using the dry olivine flow law instead of a constant viscosity of 10^{18} Pa s (implying a general increase in viscosity), the connection between the magmatic segments is initially impeded, but once it has been established, an inclined ridge-transform fault system is favoured over an orthogonal system (e.g. models *d4cm* and *e4dT*, cf. Table 1; see also Gerya, 2013).
- The imposed temperature at the bottom of the model domain has a positive correlation with the size of the magma chambers and the thickness of the newly created crust. High temperatures also favour the development of curved ridges at intermediate spreading rates (compare e.g. models *e4cm* and *e4dT*, cf. Table 1).

4. Discussion: asymmetric spreading and detachment faults

Escartín et al. (2008) denoted asymmetric accretion involving an active detachment fault as “one of the two contrasting modes of accretion” along the Mid-Atlantic Ridge in particular and along slow-spreading ridges in general. The term “detachment fault” was in this paper used for long-lived normal faults that accommodate about 50% of extension. Macleod et al. (2009) used a stricter definition. The authors reserved the term for the “very-large-offset extensional faults (...) that form the upper surfaces of uplifted oceanic core complex (OCC) massifs”. We will use the term “detachment fault” for large-

offset normal faults on or close to the axis of mid-ocean ridges that constitute the plate boundary.

In this study, asymmetrically accreting mid-ocean ridges were generated at full spreading rates of about 20 mm/yr (for $Nu = 2$, but also at higher spreading rates for larger Nu , cf. Fig. 8). Extension in the models is partly accommodated on a detachment fault situated close to the axis (Fig. 5a–b), but the ridge structure deviates from natural observations (Allerton et al., 2000) and previous numerical models (Buck et al., 2005; Tucholke et al., 2008) in two aspects:

1. The modelled detachment faults emerge atop the magma chambers, but this arrangement is transient. Stable faults dip outward (i.e. away from the ridge axis), hence new crust is mainly accreted to the footwall.
2. The magma chamber is not stationary. It is dragged towards the detachment fault and thus moves with the retreating plate.

Macleod et al. (2009) presented the life cycle of an initially inward-dipping detachment fault along a magma-starved mid-ocean ridge segment. Due to continuing spreading, the fault migrates over the temporarily starved magma chamber. When magmatic accretion resumes, new crust is added to the footwall. According to the authors, the outward-dipping detachment fault is terminated “when the supply of melt delivered to the footwall is sufficient to cut it completely”.

This mechanism is very similar to what we observed in the models of this study (Fig. 5a–b). A reason for the stability of the outward-dipping system might be that diking was not implemented in the numerical algorithm. Although most previous models assumed stationary magma chambers, we believe that the movement of magma chambers as observed in our asymmetrically accreting models might be an important mechanism. It could help explaining the very large offsets observed at certain transform faults in nature.

Buck et al. (2005) and Tucholke et al. (2008) showed that long-lived detachment faults occur at intermediate levels of magma supply, when magmatic accretion accommodates about 50% of extension. The exposure of lower crust and mantle to the sea floor (Fig. 3c) is a typical feature of OCCs (Olive et al., 2010), which mainly arise at segment ends, where melt supply is reduced compared to segment centres (Tucholke et al., 1998). In this study, very-large-offset detachment faults mainly formed in amagmatic zones between ridge segments (Fig. 3c). As the

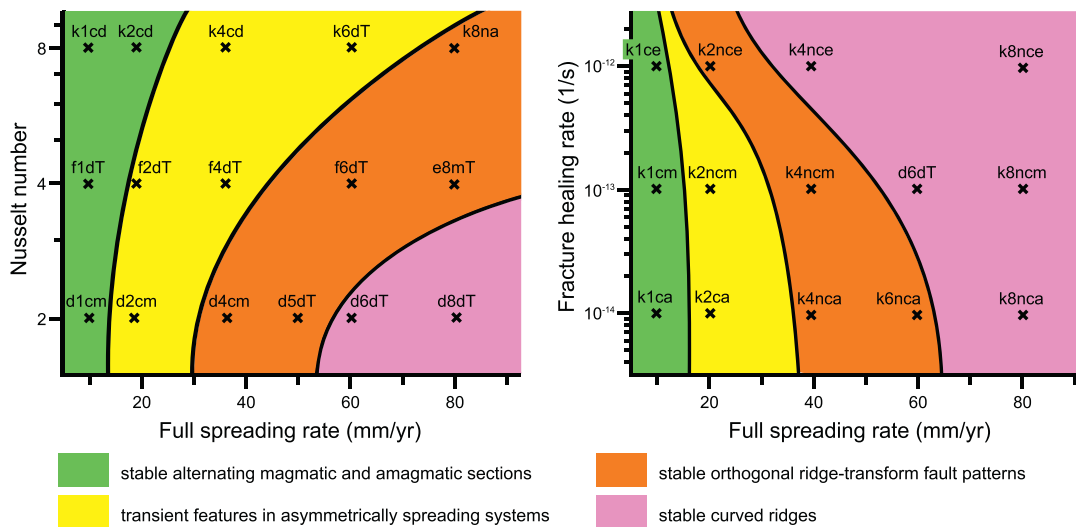


Fig. 8. Left panel: Dependence of long-term ridge morphologies on spreading rate and Nu . All models in the diagram have a fracture healing rate of 10^{-13} s^{-1} , constant viscosity of 10^{18} Pa s in the asthenosphere and an initial crustal thickness of 7 km. Right panel: Dependence of long-term ridge morphologies on spreading rate and $\dot{\epsilon}_{\text{healing}}$. All models in the diagram have $Nu = 2$, constant viscosity of 10^{18} Pa s in the asthenosphere and an initial crustal thickness of 7 km. See Table 1 for more details.

melt supply in our models does not vary along-axis, the situation at segment ends is not different from segment centres. Detachment faults extend laterally up to 50 km, and structures similar to OCCs can form along the entire ridge segment.

The lifetime of faults in our models decreases with increasing spreading rate (and thus increasing level of magma supply). Axial faults are also observed in symmetrically spreading ridge models, but these structures are short-lived and frequently abandoned (Fig. 5c). The resulting structures accordingly have short wavelengths and are indeed very similar to abyssal hills, the most prominent feature of slow-spreading mid-ocean ridge flanks (Buck et al., 2005). As in the 2-D studies by Buck et al. (2005) and Tucholke et al. (2008), features resembling OCCs and abyssal hills are thus in our models generated by the same mechanism.

5. Comparison with nature and conclusions

Ultraslow-spreading ridges on Earth consist of alternating magmatic and amagmatic segments and lack transform faults. This finding by Dick et al. (2003) could be reproduced numerically. According to our model results, amagmatic segments replace transform faults at these rates of extension, which is a possible explanation for why the latter are not observed at ultraslow ridges in nature. In amagmatic segments, extension is accommodated by enhanced fracturing and crustal thinning. In accordance with the observations by Dick et al. (2003), the mantle is exposed to the seafloor over large regions.

In accordance with observations of natural ultraslow-spreading ridges, topography of the magmatic segments is very rough, the ridge flanks are elevated and the ridge axis is depressed. The ridge axis of the magmatic segments is oriented perpendicularly to the direction of spreading. In the amagmatic region, the ridge is defined by a depressed region connecting the magmatic segments, which however only appears for moderate offsets (max. 30 km) between the spreading centres. As observed by Dick et al. (2003) in the Southwest Indian Ridge, the modelled ridge is oblique to the direction of spreading in the magma-starved regions, but its topography is too poor.

The lack of transform faults in ultraslow-spreading ridge models can be explained by the relative dominance of fracture healing with respect to fracture weakening. While weakening depends on the rate of extension, healing is described by the constant parameter $\dot{\epsilon}_{\text{healing}}$ (cf. Appendix B). As fractures at very low spreading rates heal quickly relative to the other dynamics, the initialized offset magmatic segments cannot lengthen by ridge propagation. But just like transform faults, the evolving amagmatic zones represent a zone of depressed isotherms and accordingly reduced production of melt in the mantle underneath, and melt escapes towards the hotter magmatic segments (Montési and Behn, 2007).

Natural slow-spreading ridges show the typical perpendicular orientation of magmatic segments and transform faults (Macdonald, 2001). Transform fault, inactive fracture zone and ridge axis are depressed, the elevated flanks of the ridge are marked by ridge-parallel abyssal hills. All these features were reproduced numerically in the study by Gerya (2013). This study confirms his results for spreading velocities of about 40 mm/yr.

Natural fast-spreading ridges are characterized by a smooth topography and axial highs (Dick et al., 2003). The smooth topography is reproduced in the experiments. As spreading is symmetric and fully magmatic, there are no fault scarps on the ridge flanks. In contrast to nature, there is no axial high. The ridge axis is gently depressed with respect to the flanking highs, but it is shallower than the sea floor on the distal sides of the flanking highs. Naar and Hey (1989) report an upper limit for the stability of transform faults at spreading rates > 145 mm/yr. In the experiments, this limit is reached at much lower spreading rates of about 60 mm/yr (depending also on the amount of hydrothermal cooling, cf. Fig. 8). Magmatic segments in the experiments bend towards each other, coalesce and form a curved ridge.

This behaviour can be explained by elevated isotherms beneath the transform fault when compared to slow-spreading ridge models. Due to the higher temperatures, the production of melt increases, and melts start to accrete to the bottom of the transform fault, thereby terminating it.

A systematic sensitivity analysis revealed that Nu (describing the extent of hydrothermal circulation) and $\dot{\epsilon}_{\text{healing}}$ (describing the fracture healing process) have a significant influence on the resulting ridge morphology and shift the occurrence of the four regimes presented above to different spreading rates (Fig. 8). With $Nu = 8$, orthogonal ridge-transform systems are only stable at spreading rates > 60 mm/yr, and the ridge-parallel hill structures that dominate the topography at lower Nu (for spreading rates between 20 mm/yr and 60 mm/yr) disappear. Since orthogonal ridge-transform systems and ridge-parallel hill structures are observed at slow spreading rates in nature (e.g. Macdonald, 2001), we believe that values for Nu between 2 and 4 are more realistic in natural systems.

In models with $\dot{\epsilon}_{\text{healing}} = 10^{-12} \text{ s}^{-1}$, orthogonal ridge-transform systems are only stable for a narrow range of spreading rates of about 20 mm/yr. But as transform faults in nature are observed at a much wider range of spreading rates (e.g. Macdonald, 2001), we expect fracture healing rates of 10^{-14} s^{-1} – 10^{-13} s^{-1} in natural mid-ocean ridge systems. Taken the grid resolution dependence of the healing rate (Appendix B), it is better to interpret it in terms of the critical slip rate on a fault, which is a minimum time-averaged slip rate required to accumulate damage and cause weakening of the fault (Gerya, 2013). Thus, according to our models, in natural mid-ocean ridge systems this critical time-averaged slip rate varies in the range of 0.3–3 mm/yr.

We have shown the current possibilities and limitations of 3-D thermomechanical mid-ocean ridge modelling. While the most prominent features of ultraslow- and slow-spreading ridges could be reproduced numerically, this has not been possible for fast-spreading ridges. This study can also help to understand the mechanisms of faulting at slow-spreading ridges, although the processes leading to structurally similar features in models and nature might differ in detail. Asymmetric accretion involving a lateral migration of the ridge segment as observed in models of this study might be an explanation for very large offsets observed at certain transform faults in nature.

We also investigated the sensitivity of our model results on the fracture healing rate $\dot{\epsilon}_{\text{healing}}$ and the Nusselt number for hydrothermal circulation Nu . In order to analyse whether our preferred values for these parameters represent realistic values for natural systems, more investigations of the interplay with other parameters are necessary. Further efforts will concentrate on generating more realistic numerical models of mid-ocean ridges. Future implementations might include elastic effects, diking and percolation of magma, as well as higher resolutions both in space and time.

Acknowledgements

We thank Prof. G. Ito and an anonymous reviewer for constructive comments on the manuscript. This work was supported by ETH Research Grant ETH-0609-2, SNF ProDoc program 4-D-Adamello, and Crystal2Plate program.

Appendix A. Modelling of mid-ocean ridge processes

The numerical model is more complex than in previous 3-D numerical modelling approaches (Choi et al., 2008; Gerya, 2010a; Allken et al., 2011, 2012). This is mainly dictated by the necessity to address a relatively complex and long-lasting transition between the plate breakup and oceanic spreading. Thus, long-term crustal and lithospheric deformation, accretion and cooling processes have to be captured (e.g. Buck et al., 2005; Olive et al., 2010) to allow for a direct comparison of the numerical results with crustal faulting, growth and topography patterns observed in incipient and mature oceanic spreading regions (e.g. Dick

et al., 2003; Macleod et al., 2009; Taylor et al., 2009). Therefore, the conceptual model accounts for the following key processes that were suggested to be critical for realistic modelling of plate breakup and oceanic spreading (e.g. Buck et al., 2005; Gregg et al., 2009; Katz, 2010; Olive et al., 2010; Theissen-Krah et al., 2011):

- (i) Thermal accretion of the oceanic mantle lithosphere resulting in plate thickness growth
- (ii) Partial melting of the asthenospheric mantle, melt extraction and percolation towards the ridge resulting in crustal growth
- (iii) Crystallization of the new oceanic crust beneath the ridge
- (iv) Hydrothermal circulation at the axis of the ridge resulting in excess cooling of the crust.

These physical processes are included in our numerical model in a simplified manner, as described in more detail below.

Thermal accretion of the mantle lithosphere is modelled by solving the heat conduction equation combined with a temperature-dependent viscosity for the non-molten mantle (dry olivine flow law, Ranalli, 1995). Consequently, cooling asthenospheric mantle becomes rheologically strong and accretes spontaneously to the bottom of the oceanic lithosphere.

Hydrothermal circulation at the axis of the ridge producing rapid cooling of the new oceanic crust (e.g. Theissen-Krah et al., 2011) is parameterised with an enhanced thermal conductivity of the crust based on the following equation (Gregg et al., 2009):

$$k_{\text{eff}} = k + k_0(Nu - 1) \exp \left[A \left(2 - \frac{T}{T_{\text{max}}} - \frac{y}{y_{\text{max}}} \right) \right], \quad (\text{A.1})$$

where k is the thermal conductivity of dry rocks, $k = (0.73 + \frac{1293}{T/K+77}) \frac{\text{W}}{\text{mK}}$ for the mantle and $k = (1.18 + \frac{474}{T/K+77}) \frac{\text{W}}{\text{mK}}$ for the crust (after Clauser and Huenges, 1995), and $k_0 = 3 \frac{\text{W}}{\text{mK}}$ is the reference thermal conductivity. Nu is the assumed Nusselt number for hydrothermal circulation, $A = 0.75$ is a smoothing factor, T is temperature, $T_{\text{max}} = 873 \text{ K}$ is the cut-off maximum temperature, y is depth and $y_{\text{max}} = 6 \text{ km}$ is the cut-off maximum depth. Following the suggestion by Gregg et al. (2009), values for Nu between 2 and 8 are tested in this study. In order to insure an efficient heat transfer from the upper surface of the plate in the Eulerian model, thermal conductivity of the sea water layer above this plate is taken to be hundred times higher ($200 \frac{\text{W}}{\text{mK}}$) than that of the dry mantle ($1-4 \frac{\text{W}}{\text{mK}}$).

Partial melting of the asthenospheric mantle, melt extraction and percolation towards the ridge is implemented in a highly simplified manner. According to our model, crustal growth at the ridge is balanced by the melt production and extraction in the mantle. However, melt percolation towards the ridge (e.g. Katz, 2010) is not modelled directly and considered to be nearly instantaneous (Connolly et al., 2009). The standard (i.e. without melt extraction) volumetric degree of mantle melting M_0 changes with pressure and temperature according to the parameterised batch melting model of Katz et al. (2003). Lagrangian markers track the amount of melt extracted during the evolution of each experiment. The total amount of melt M for every marker takes into account the amount of previously extracted melt and is calculated as (Nikolaeva et al., 2008)

$$M = M_0 - \sum_{i=1}^n M_i^{\text{ext}}, \quad (\text{A.2})$$

where M_i^{ext} is the melt fraction extracted in the i th extraction episode. The rock is considered non-molten (refractory) when the extracted melt fraction is larger than the standard one (i.e. when $\sum M_i^{\text{ext}} > M_0$). If the total amount of melt M for a given marker is larger than zero, the melt fraction M is extracted and $\sum M_i^{\text{ext}}$ is updated. The extracted melt fraction M is assumed to propagate much faster than the plates deform (Connolly et al., 2009). This assumption justifies the instantaneous transmission of

extracted melt to the magma chamber. Similarly to Gregg et al. (2009), a wide pooling region for melt extraction is assumed (i.e. melt can propagate across transform faults). Melts produced in the model are added evenly to the top of the shallowest regions where mantle melting conditions are still achieved. These shallowest partially molten mantle regions are typically located beneath the ridge axis and inside intra-transform spreading centres, where wedge-shaped magma chambers form spontaneously by accumulation of added melts. Size and shape of the magma chambers are regulated by the dynamics of melt supply from the bottom, crustal extension at the top and magma crystallization in response to cooling from the walls. No flow field divergence is created in response to melt accretion to the bottom of the magma chambers. Additional space for the melt is assumed to be created by viscous compaction and subsidence of the melt-bearing mantle. In order to ensure melt volume conservation and to account (indirectly) for mantle compaction and subsidence in response to the melt extraction, melt addition to the bottom of the magma chamber is done at every time step by converting the shallowest markers of hot partially molten mantle into melt markers. The total volume of these melt markers matches the total volume of extracted melt computed for the time step.

Crystallization of the new oceanic crust is modelled by spontaneous cooling and crystallization of melts at the walls of the lower-crustal magma regions (e.g. Wanless and Shaw, 2012). This simple crust accretion algorithm does not account for volcanic and plutonic (e.g. diking, Buck et al., 2005; Wanless and Shaw, 2012) processes above the magma regions, neither does it account for internal convection, melt segregation and crystal differentiation inside these regions (Wanless and Shaw, 2012). The effective density of molten crust in the magma chamber is calculated as

$$\rho_{\text{eff}} = \rho_{\text{solid}} \left(1 - M + M \frac{\rho_{0,\text{molten}}}{\rho_{0,\text{solid}}} \right), \quad (\text{A.3})$$

where the local melt fraction M is computed from the simple linear batch melting model (Gerya, 2010b)

$$M = 0 \text{ for } T < T_{\text{solidus}}, \quad (\text{A.4})$$

$$M = \frac{T - T_{\text{solidus}}}{T_{\text{liquidus}} - T_{\text{solidus}}} \text{ for } T_{\text{solidus}} < T < T_{\text{liquidus}}, \quad (\text{A.5})$$

$$M = 1 \text{ for } T > T_{\text{liquidus}}. \quad (\text{A.6})$$

Here, $T_{\text{solidus}} = 1327 \text{ K} + 0.091 \frac{\text{K}}{\text{MPa}} P$ and $T_{\text{liquidus}} = 1423 \text{ K} + 0.105 \frac{\text{K}}{\text{MPa}} P$ are, respectively, solidus and liquidus temperatures of the crust at a given pressure P (Hess, 1989). $\rho_{0,\text{solid}} = 3000 \text{ kg/m}^3$ and $\rho_{0,\text{molten}} = 2800 \text{ kg/m}^3$ are the standard densities of solid and molten crust, respectively. ρ_{solid} is the density of solid crust at given P and T computed from

$$\rho_{\text{solid}} = \rho_{0,\text{solid}} [1 - \alpha(T - 298 \text{ K})] (1 + \beta(P - 0.1 \text{ MPa})), \quad (\text{A.7})$$

where $\alpha = 3 \cdot 10^{-5} \text{ K}^{-1}$ and $\beta = 10^{-5} \text{ MPa}^{-1}$ are thermal expansion and compressibility of the crust, respectively. The effect of latent heating due to equilibrium crystallization of the crust from the magma chamber is included implicitly by increasing the effective heat capacity $C_{p,\text{eff}}$ and the thermal expansion α_{eff} of the partially crystallized/molten rocks ($0 < M < 1$), calculated as (Gerya, 2010b):

$$C_{p,\text{eff}} = C_p + Q_L \left(\frac{\partial M}{\partial T} \right)_{P=\text{const}}, \quad (\text{A.8})$$

$$\alpha_{\text{eff}} = \alpha + \rho \frac{Q_L}{T} \left(\frac{\partial M}{\partial P} \right)_{T=\text{const}}, \quad (\text{A.9})$$

where $C_p = 1000 \frac{\text{J}}{\text{kg}}$ is the heat capacity of the solid crust and $Q_L = 380 \frac{\text{kJ}}{\text{kg}}$ is the latent heat of crystallization of the crust (Turcotte and Schubert, 2002). The employed linear crustal crystallization algorithm is simplified and neglects non-linearity of the melt fraction decrease with decreasing temperature between T_{liquidus} and T_{solidus} . However, this simplification should mainly affect melt crystallization dynamics inside a relatively small lower-crustal magma region without having dominant effects on the rheological and density structure of the entire model.

Appendix B. Rheological model

The model implies viscous rheology for the partially molten asthenosphere and visco-plastic rheology for the lithospheric plates. Two different viscosity models were applied for the asthenosphere. For the majority of experiments, constant viscosity of 10^{18} Pa s was prescribed. An alternative setup with a realistic temperature and strain rate dependent viscosity computed according to experimentally determined flow laws (Ranalli, 1995) was tested in specific experiments. Dry olivine flow law was used for the mantle lithosphere (and, in case, for the asthenosphere), plagioclase (An_{75}) flow law for the crust (Ranalli, 1995). Upper cut-off viscosity limits of 10^{22} Pa s– 10^{24} Pa s and lower cut-off viscosity limits of 10^{17} Pa s– 10^{18} Pa s were applied for the lithosphere. Compared to previous models of mid-ocean ridges (Hieronymus, 2004; Buck et al., 2005; Choi et al., 2008), this rheological model does not account for elasticity of the lithosphere and neglects thermally induced stresses.

Standard brittle/plastic rheology of solid rocks assumes fracture-related strain weakening (Lavie et al., 2000; Huismans and Beaumont, 2002; Hieronymus, 2004; Choi et al., 2008; Gerya, 2010a; Allken et al., 2011, 2012) and is implemented by using a plate strength limitation in the form

$$\sigma_{II} \leq C_\gamma + \phi_\gamma (P - P_f), \quad (\text{B.1})$$

where σ_{II} is the second invariant of the stress tensor, $\sigma_{II} = \sqrt{\frac{1}{2}(\sigma'_{ij})^2}$, P is dynamic pressure on solids and $P_f = \rho_f g y$ is fluid pressure ($\rho_f = 1000 \text{ kg/m}^3$ is water density, $g = 9.81 \text{ m/s}^2$ is gravity, and y is the vertical coordinate). The parameters C_γ and ϕ_γ are cohesion and coefficient of inner friction, respectively, and are defined in the following way:

$$\phi_\gamma = 1, \quad P < P_f \quad (\text{tensile fracture}), \quad (\text{B.2})$$

$$\phi_\gamma = 0.6 \left(1 - \frac{\gamma}{\gamma_0}\right) \quad \text{for } \gamma \leq \gamma_0 \quad \text{and} \quad \phi_\gamma = 0 \quad (\text{B.3})$$

for $\gamma > \gamma_0$, $P \geq P_f$ (confined fracture).

$$C_\gamma = C_0 + (C_1 - C_0) \frac{\gamma}{\gamma_0} \quad \text{for } \gamma \leq \gamma_0 \quad \text{and} \quad C_\gamma = C_1 \quad \text{for } \gamma > \gamma_0. \quad (\text{B.4})$$

$\gamma \geq 0$ is here the integrated plastic strain ($\gamma_0 = 1$ is the upper strain limit for fracture related weakening) and can be calculated via

$$\gamma = \int \sqrt{\frac{1}{2}(\dot{\epsilon}_{ij(\text{plastic})})^2} dt - \int \dot{\epsilon}_{\text{healing}} dt. \quad (\text{B.5})$$

here, $\dot{\epsilon}_{ij(\text{plastic})}$ is the plastic strain rate tensor and $\dot{\epsilon}_{\text{healing}}$ is fracture healing rate. C_0 and C_1 in Eq. (B.4) are the initial and final strength values for fracture-related weakening, respectively. Maximal strain along active faults in our models is always greater than 1. Therefore, maximal amount of fault strain weakening corresponds to $\phi_\gamma = 0$ and $C_\gamma = C_1$ in Eq. (B.1).

The stress limitation for tensile fracture was formulated from a theoretical criterion (Rozhko et al., 2007) for tensile failure of a fluid-filled crack. This criterion is based on Griffith's theory (Murrell, 1964) and has been verified experimentally (Jaeger, 1963). Strain weakening assumed in the model is similar to that in previous numerical studies

of mid-ocean ridges (e.g. Hieronymus, 2004; Choi et al., 2008; Gerya, 2010a) and continental rifting (Huismans and Beaumont, 2002; Allken et al., 2011). It is related, in particular, to water and melt percolation and textural modifications along fault zones and their intense serpentinisation that strongly decreases the strength of fractured fault rocks (Escartín et al., 2001; Huismans and Beaumont, 2002; Hilaret et al., 2007; Bercovici and Ricard, 2012). Partial healing of deactivated slowly creeping fractures (Lyakhovskiy and Ben-Zion, 2008) was applied by using an imposed healing rate $\dot{\epsilon}_{\text{healing}}$ that reduces accumulated plastic strain γ with time, tested values for $\dot{\epsilon}_{\text{healing}}$ were in the range between 0 and 10^{-13} s^{-1} (Table 1).

If the second invariant of the local plastic strain rate tensor $\dot{\epsilon}_{II,\text{plastic}} = \sqrt{\frac{1}{2}(\dot{\epsilon}'_{ij,\text{plastic}})^2}$ inside a fault is greater than $\dot{\epsilon}_{\text{healing}}$, the accumulated strain γ increases with time according to Eq. (B.5) and the brittle-plastic strength decreases according to Eqs. (B.3)–(B.4). In contrast, if $\dot{\epsilon}_{II,\text{plastic}} < \dot{\epsilon}_{\text{healing}}$, the accumulated strain γ starts to decrease according to Eq. (B.5) and brittle-plastic strength recovery of the fault occurs according to Eqs. (B.3)–(B.4). This simple brittle/plastic weakening/healing model, in which γ serves as a damage/recovery measure, implies that the magnitude of healing rate $\dot{\epsilon}_{\text{healing}}$ should be comparable with the magnitude of the strain rate $\dot{\epsilon}'_{ij,\text{plastic}}$ inside active faults.

Taken that spontaneously forming brittle/plastic faults are localized on one to two grid cells, both strain weakening limit γ_0 and healing rate $\dot{\epsilon}_{\text{healing}}$ should linearly scale with the grid step size (e.g. Lavie et al., 2000). This scaling makes the weakening and healing to be dependent on the absolute amount of material displacement along the walls of spontaneously forming faults irrespective of the numerical resolution (e.g. Lavie et al., 2000). In particular, the adopted $\gamma_0 = 1$ value implies 1000 m of relative displacement ($d = 2\gamma_0\Delta x$, where $\Delta x = 500 \text{ m}$ is the model grid step) between the walls of a fault. Similarly, the adopted $\dot{\epsilon}_{\text{healing}} = 10^{-13} \text{ s}^{-1}$ used in most experiments (Table 1) implies brittle/plastic strength recovery for displacement rates of less than 3 mm/yr ($2\dot{\epsilon}_{\text{healing}}\Delta x = 10^{-10} \text{ m/s}$) between the walls of a fault.

It should be pointed out that the employed simple strain weakening/healing model (Lavie et al., 2000; Huismans and Beaumont, 2002; Hieronymus, 2004; Lyakhovskiy and Ben-Zion, 2008; Choi et al., 2008; Gerya, 2010a; Allken et al., 2011, 2012) is purely phenomenological and does not directly reflect the physics involved in various weakening/healing processes. These processes may in particular involve fluid and melt percolation, grain damage and growth, structural annealing and Zener pinning in multi-phase polycrystalline lithospheric rocks (e.g. Bercovici and Ricard, 2012). Therefore, theoretical development (e.g. Bercovici and Ricard, 2012) and numerical implementation of more sophisticated and realistic lithospheric weakening/healing models are required in the future.

References

- Allerton, S., Escartín, J., Searle, R.C., 2000. Extremely asymmetric magmatic accretion of oceanic crust at the ends of slow-spreading ridge segments. *Geology* 28, 179–182.
- Allken, V., Huismans, R.S., Thieulot, C., 2011. Three-dimensional numerical modeling of upper crustal extension systems. *Journal of Geophysical Research* 116, B10409.
- Allken, V., Huismans, R.S., Thieulot, C., 2012. Factors controlling the mode of rift interaction in brittle-ductile coupled systems: a 3D numerical study. *Geochemistry, Geophysics, Geosystems* 13.
- Behn, M.D., Lin, J., Zuber, M.T., 2002. Evidence for weak oceanic transform faults. *Geophysical Research Letters* 29. <http://dx.doi.org/10.1029/2002GL015612>.
- Bercovici, D., Ricard, Y., 2012. Mechanisms for the generation of plate tectonics by two-phase grain-damage and pinning. *Physics of the Earth and Planetary Interiors* 202–203, 27–55.
- Buck, W.R., Lavie, L.L., Poliakov, A.N.B., 2005. Modes of faulting at mid-ocean ridges. *Nature* 434, 719–723.
- Cann, J.R., Blackman, D.K., Smith, D.K., McAllister, E., Janssen, B., Mello, S., Avgerinos, E., Pascoe, A.R., Escartín, J., 1997. Corrugated slip surfaces formed at north atlantic ridge-transform intersections. *Nature* 385, 329–332.
- Choi, E., Lavie, L., Gurnis, M., 2008. Thermomechanics of mid-ocean ridge segmentation. *Physics of the Earth and Planetary Interiors* 171, 374–386.

- Clauser, C., Huenges, E., 1995. Thermal conductivity of rocks and minerals. *Rock Physics and Phase Relations: American Geophysical Union*, pp. 105–126.
- Connolly, J.A.D., Schmidt, M.W., Solferino, G., Bagdassarov, N., 2009. Permeability of asthenospheric mantle and melt extraction rates at mid-ocean ridges. *Nature* 462, 209–212.
- Dauteuil, O., Bourgeois, O., Mauduit, T., 2002. Lithosphere strength controls oceanic transform zone structure: insights from analogue models. *Geophysical Journal International* 150, 706–714.
- Dick, H.J.B., Lin, J., Schouten, H., 2003. An ultraslow-spreading class of ocean ridge. *Nature* 426, 405–412.
- Escartín, J., Hirth, G., Evans, B., 2001. Strength of slightly serpentinized peridotites: implications for the tectonics of oceanic lithosphere. *Geology* 29, 1023–1026.
- Escartín, J., Smith, D.K., Cann, J., Schouten, H., Langmuir, C.H., Escrig, S., 2008. Central role of detachment faults in accretion of slow-spreading oceanic lithosphere. *Nature* 455, 790–794.
- Gerya, T.V., 2010a. Dynamical instability produces transform faults at mid-ocean ridges. *Science* 329, 1047–1050.
- Gerya, T.V., 2010b. Introduction to Numerical Geodynamic Modelling. Cambridge University Press.
- Gerya, T.V., 2012. Origin and models of oceanic transform faults. *Tectonophysics* 522, 34–54.
- Gerya, T.V., 2013. Three-dimensional thermomechanical modeling of oceanic spreading initiation and evolution. *Physics of the Earth and Planetary Interiors* 214, 35–52.
- Gerya, T.V., Yuen, D.A., 2007. Robust characteristic method for modeling multiphase visco-elasto-plastic thermo-mechanical problems. *Physics of the Earth and Planetary Interiors* 163, 83–105.
- Gregg, P.M., Behn, M.D., Lin, J., Grove, T.L., 2009. Melt generation, crystallization, and extraction beneath segmented oceanic transform faults. *Journal of Geophysical Research* 114. <http://dx.doi.org/10.1029/2008JB006100>.
- Hess, P.C., 1989. *Origin of Igneous Rocks*. Harvard University Press.
- Hieronymus, C.F., 2004. Control on seafloor spreading geometries by stress- and strain-induced lithospheric weakening. *Earth and Planetary Science Letters* 222, 177–189.
- Hilaliret, N., Reynard, B., Wang, Y., Daniel, I., Merkel, S., Nishiyama, N., Petitgirard, S., 2007. High-pressure creep of serpentine, interseismic deformation and initiation of subduction. *Science* 318, 1910–1913.
- Huisman, R.S., Beaumont, C., 2002. Asymmetric lithospheric extension: the role of frictional plastic strain softening inferred from numerical experiments. *Geology* 30, 211–214.
- Ito, G., Behn, M., 2008. Magmatic and tectonic extension at mid-ocean ridges: 2. origin of axial morphology. *Geochemistry, Geophysics, Geosystems* 9. <http://dx.doi.org/10.1029/2008GC001970>.
- Jaeger, J.C., 1963. Extension failures in rocks subject to fluid pressure. *Journal of Geophysical Research* 68, 6066.
- Kappel, E., Ryan, W., 1986. Volcanic episodicity and a non-steady state rift valley along northeast pacific spreading centers: evidence from Sea MARC I. *Journal of Geophysical Research* 91, 13925–13940.
- Katz, R.F., 2010. Porosity-driven convection and asymmetry beneath mid-ocean ridges. *Geochemistry, Geophysics, Geosystems* 11. <http://dx.doi.org/10.1029/2010GC003282>.
- Katz, R.F., Spiegelman, M., Langmuir, C.H., 2003. A new parameterization of hydrous mantle melting. *Geochemistry, Geophysics, Geosystems* 4, 1073.
- Lavier, L.L., Buck, W.R., Poliakov, A.N.B., 2000. Factors controlling normal fault offset in an ideal brittle layer. *Journal of Geophysical Research* 105, 23431–23442.
- Lyakhovskiy, V., Ben-Zion, Y., 2008. Scaling relations of earthquakes and aseismic deformation in a damage rheology model. *Geophysical Journal International* 172, 651–662.
- Macdonald, K.C., 2001. Mid-ocean ridge tectonics, volcanism and geomorphology. *Encyclopedia of Ocean Sciences*. Academic Press, pp. 1798–1813.
- Macleod, C.J., Searle, R.C., Murton, B.J., Casey, J.F., Mallows, C., Unsworth, S.C., Achenbach, K.L., Harris, M., 2009. Life cycle of oceanic core complexes. *Earth and Planetary Science Letters* 287, 333–344.
- Montési, L., Behn, M., 2007. Mantle flow and melting underneath oblique and ultraslow mid-ocean ridges. *Geophysical Research Letters* 34. <http://dx.doi.org/10.1029/2007GL031067>.
- Murrell, S.A.F., 1964. The theory of propagation of elliptical griffith cracks under various conditions of plane strain or plain stress. *British Journal of Applied Physics* 15, 1123.
- Naar, D.F., Hey, R.N., 1989. Speed limit for oceanic transform faults. *Geology* 17, 420–422.
- Nikolaeva, K., Gerya, T.V., Connolly, J.A.D., 2008. Numerical modelling of crustal growth in intraoceanic volcanic arcs. *Physics of the Earth and Planetary Interiors* 171, 336–356.
- Oldenburg, D.W., Brune, J.N., 1972. Ridge transform fault spreading pattern in freezing wax. *Science* 178, 301.
- Olive, J., Behn, M.D., Tucholke, B.E., 2010. The structure of oceanic core complexes controlled by the depth distribution of magma emplacement. *Nature Geoscience* 3, 491–495.
- Phipps Morgan, J., Chen, Y., 1993. Dependence of ridge-axis morphology on magma supply and spreading rate. *Nature* 364, 706–708.
- Ranalli, G., 1995. *Rheology of the Earth*. Chapman & Hall.
- Rozhko, A.Y., Podladchikov, Y.Y., Renard, F., 2007. Failure patterns caused by localized rise in pore-fluid overpressure and effective strength of rocks. *Geophysical Research Letters* 34, L22304.
- Taylor, B., Goodliffe, A., Martinez, F., 2009. Initiation of transform faults at rifted continental margins. *Comptes Rendus Geoscience* 341, 428–438.
- Theissen-Krah, S., Iyer, K., Rüpkke, L.H., Phipps Morgan, J., 2011. Coupled mechanical and hydrothermal modeling of crustal accretion at intermediate to fast spreading ridges. *Earth and Planetary Science Letters* 311, 275–286.
- Tucholke, B., Lin, J., Kleinrock, M., 1998. Megamullions and mullion structure defining oceanic metamorphic complexes on the mid-atlantic ridge. *Journal of Geophysical Research* 103, 98579866.
- Tucholke, B.E., Behn, M.D., Buck, W.R., Lin, J., 2008. Role of melt supply in oceanic detachment faulting and formation of megamullions. *Geology* 36, 455–458.
- Turcotte, D.L., Schubert, G., 2002. *Geodynamics*. Cambridge University Press.
- Wanless, V.D., Shaw, A.M., 2012. Lower crustal crystallization and melt evolution at mid-ocean ridges. *Nature Geoscience* 5, 651–655.